UNIVERSIDADE DE SÃO PAULO
INSTITUTO DE FÍSICA DE SÃO CARLOS

Mateus Piovezan Otto

Searching for dark matter in the Galactic Center with the Fermi Gamma-ray Space Telescope

São Carlos

2020

Mateus Piovezan Otto

Searching for dark matter in the Galactic Center with the Fermi Gamma-ray Space Telescope

Undergraduate thesis presented to the Undergraduate Program in Physics at the São Carlos Institute of Physics, University of São Paulo, as a partial requirement to obtain the degree of Bachelor of Computational Physics.

Advisor: Prof. Dr. Aion da Escóssia de Melo Viana

São Carlos

2020

Otto, Mateus Piovezan
Searching for dark matter in the Galactic Center with the Fermi Gamma-ray Space Telescope / Mateus Piovezan Otto; advisor Aion da Escóssia de Melo Viana -- São Carlos 2020.
20 p.

Undergraduate thesis (Bachelor of Computational Physics) - Instituto de Física de São Carlos, Universidade de São Paulo, 2020.

1. Dark matter. 2. Gamma rays. 3. Data analysis. 4. Galactic center. I. da Escóssia de Melo Viana, Aion, advisor. II. Title.

Abstract

It is generally accepted nowadays that the matter density of the Universe mainly consists of an unknown component, called Dark Matter (DM). It is also believed that DM is formed of a new neutral, stable and non-baryonic elementary particle. In high density environments of the Universe, DM may self-annihilate and produce a strong gamma ray signal. Among all possible targets, the Galactic Center region is expected to be the brightest source of DM annihilations in the gamma ray sky by several orders of magnitude. This project aims to study and characterize the gamma ray emission of the Galactic Center region as seen by the Fermi Large Area Telescope (Fermi-LAT), on board of the Fermi Gamma Ray Space Telescope spacecraft. Since this region also has a strong astrophysical non-thermal gamma ray emission, a particular attention will be given to the subtraction of the most up-to-date background models in order to recover the famous residual *Galactic Center GeV Excess* and interpret it in terms of a DM self-annihilation signal.

Keywords: Dark matter. Gamma rays. Data analysis. Galactic center.

Contents

1 The need for dark matter

The historical basis of the dark matter paradigm can be traced back to the early 1930s, when Fritz Zwicky, a Swiss astronomer, began a systematic research of the redshifts of galaxies in some galaxy clusters, including the Virgo, Leo and Coma ones. At his seminal article (1), Zwicky found that the velocity dispersion of the components of the Coma Cluster, as measured from the deviation of the mean velocity, could not be explained if the cluster was in dynamical equilibrium. In order to match the observations, he was forced to conclude that the total matter density of the cluster needed to be approximately 400 times greater than the luminous matter density. It was Zwicky who coined the term *dark matter* (DM) for the apparently non-luminous mass component that needed to exist to fulfill the observed density gap.

Despite Zwicky's pioneering work, some astronomers (2) consider the first robust evidences of the existence of dark matter to be based on the study of spiral galaxy rotation curves. Briefly stated, a galaxy rotation curve is the measurement of the rotational velocity (v_r) of stars in the galaxy as a function of the distance from the galactic bulge.

From Newton's theory of gravitation, we know that for an star orbiting an homogeneous and spherical matter distribution with density ρ and radius R, its rotational velocity will be:

$$v_r(r) = \begin{cases} \sqrt{\dfrac{4\pi G\rho}{3}}r, & r \leq R \\ \sqrt{\dfrac{GM}{r}}, & r > R \end{cases} \tag{1}$$

so that, for $r > R$, we expect a so-called *Keplerian fall-off*: $v_r \propto r^{-\frac{1}{2}}$. Even though spiral galaxies have a disk-like shape whose gravitational potentials are much more complex than in the spherical and homogeneous case considered above, more intricate potentials (such as the Kuzmin model) result in rotational velocities (3) with the same general features: an initial and close to linear rise that is followed by an asymptotic tendency to the Keplerian fall-off.

Instead of revealing the expected decay of rotational velocities, observations indicated that the galaxy rotation curves flattens out at large distances. Figure 1 shows the 21 galaxy rotation curves measured by Vera Rubin and colleagues (4), which illustrate the approximate flattening of the rotational velocity far from the bulge.

Both Zwicky's and Rubin's work form a *dynamical* basis for the existence of dark matter.

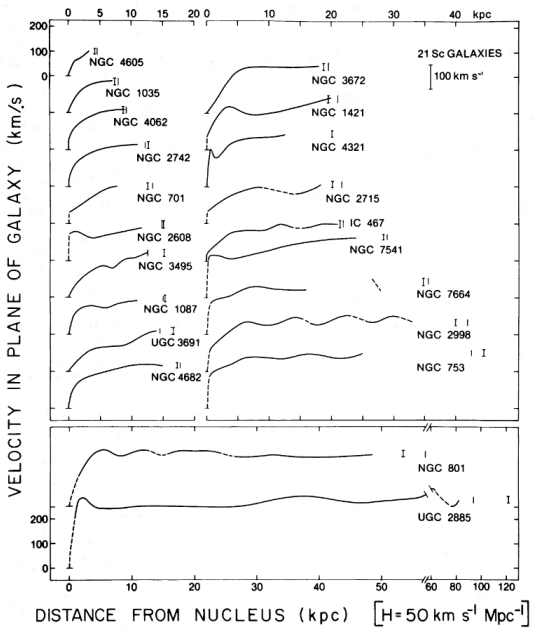

Figure 1 – Rotation curves of spiral galaxies (Sc in the Hubble system) as measured in (4). Dashed lines in the curve indicate faster than Keplerian fall-off. Source: RUBIN, V. C.; FORD W. K., J.; THONNARD, N. (4)

Nevertheless, other non-dynamical evidences has strengthen out the need for a dark component of the universe's mass. For instance, Planck results (5) based on the Cosmic Microwave Background (CMB) anisotropies predict that nearly 85% of the universe's matter density is dark.

In this work, we also focus on a non-dynamical evidence of the existence of dark matter. More specifically, we study an excess of radiation detected in the Galactic Center of the Milky Way (6) and, following early explanatory attempts (7), try to interpret it as a signal of dark matter self-annihilation.

2 Dark matter physics

2.1 Constraints from dynamical observations

We begin this section by building mild model-independent constraints on the physical and astrophysical nature of dark matter, mainly based on the dynamical traces of its existence discussed in Section 1. We restrict our attention, from now on, to the Milky Way Galaxy and on particle non-baryonic DM candidates[1]. First, we assume dark matter forms a spherical matter

[1] There are models based on baryonic dark matter, such as Massive Compact Halo Objects (MACHOs) and Primordial Black Holes (PBHs).

halo superposed to the baryonic disk-like matter distribution, as shown in Figure 2.

With this, by eq. (1), we can account for the approximate flattening of the rotation curves if, for $r \gg R_{\rm disk}$, we have that $M_{DM}(r) \propto r$, where $M_{DM}(r)$ is the total dark matter halo mass inside the radius r. In terms of the DM mass density:

$$\rho(r) \propto \frac{M(r)}{r^2} \sim \frac{1}{r^2} \tag{2}$$

Now, stellar kinematics (8) constrain the total mass of the dark matter halo to be $M \sim 10^{12}\,\mathrm{M}_\odot$ and the local DM density to be $\rho_\odot \sim 0.3$ GeV cm^{-3}. Therefore, if we suppose that the density in eq. (2) holds for the entire DM halo, we can get an estimate of its radius:

$$M_{DM} \sim 4\pi \int_0^{R_{\rm halo}} r^2 \rho(r) dr \rightarrow R_{\rm halo} \sim 100\,\mathrm{kpc} \tag{3}$$

that is one order of magnitude greater than the baryonic disk radius, $R_{\rm disk} \sim 10\,\mathrm{kpc}$. It is important to stress that this is a very rough estimate of $R_{\rm halo}$, mainly because it is not correct to think of the DM halo as having a finite radius and establishing an adequate reference for comparing halo sizes is a subtle problem (2).

Finally, by using the virial theorem, the average velocity of DM particles in the halo is:

$$\langle v \rangle = \sqrt{\frac{G M_{\rm halo}}{R_{\rm halo}}} \sim 200\,\mathrm{km/s}, \tag{4}$$

which means that DM probably exists, today, as a non-relativistic particle.

2.2 Spatial distribution

Our previous estimate of the DM density, eq. (2), relied on the assumption of a DM halo that is spherically symmetric and in dynamical equilibrium. However, much precise descriptions of the DM density arise if we leave the realm of semi-analytical calculations. Nowadays, the most accurate description of DM spatial distribution comes from numerical N-body simulations, such as `Aquarius` (9) and `Via Lactea II`, that follows structure formation since the initial DM density perturbations. These simulations, despite not tracking the baryon physics[2], initially

[2] For a deeper discussion, I refer the reader to (2).

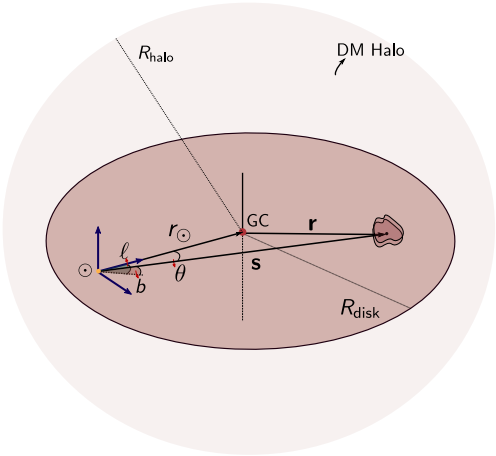

Figure 2 – Spherical dark matter halo superposed to the Milky Way disk. GC is the Galactic Center. Source: By the author.

endorsed that DM distributes according to a universal profile (10), called Navarro-Frenk-White (NFW):

$$\rho_{\text{NFW}}(r) = \rho_s \frac{r_s}{r}\left(1 + \frac{r}{r_s}\right)^{-2} \tag{5}$$

where r_s is the scale radius and $\rho_s = 4\rho_{\text{NFW}}(r_s)$ the scale density. It is called universal in the sense that for every galaxy, the DM halo has the same radial density profile. There is, however, a debate whether the Einasto profile:

$$\rho_{\text{Ein}}(r) = \rho_s \exp\left\{-\frac{2}{\alpha}\left[\left(\frac{r}{r_s}\right)^{\alpha} - 1\right]\right\} \tag{6}$$

is favored in more recent N-body simulations (9).

Additionally, the literature on experimental data analysis (11) suggests the use of a so-called generalized Navarro-Frenk-White (gNFW) profile:

$$\rho_{\text{gNFW}}(r) = \rho_s \left(\frac{r_s}{r}\right)^{-\gamma}\left(1 + \frac{r}{r_s}\right)^{-3+\gamma} \tag{7}$$

where $\gamma \approx 1.2$, indicating a steeper than NFW density closer to the galactic center. The most common profiles used in spatial modelling of the DM distribution are shown in Figure 3.

Note that, despite its greater precision, N-body simulations seems to ratify our initial hypothesis of a spherically distributed DM halo. Microscopically, this fact can be accounted for

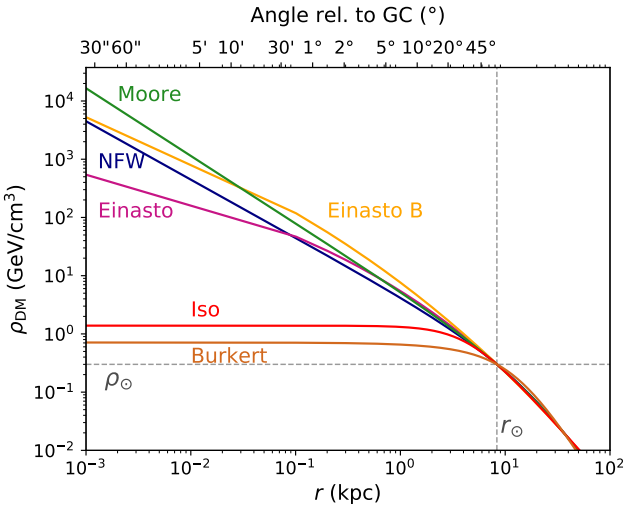

Figure 3 – Dark matter density profiles scaled for the Milky Way galaxies. Source: By the author.

if DM particles are non-collisional, thus disallowing the collapse of a spherical halo into a disk.

2.3 Annihilating dark-matter and indirect detection

Consider the case of a dark matter halo with spatial distribution given by one of the above profiles. Our objective is to describe the expected signal if DM particles in this halo, henceforth denoted as χ, annihilate to a Standard Model (SM) species X. The process is depicted in Figure 4. Note that we are explicitly considering the case of self-annihilating dark matter ($\chi = \bar{\chi}$).

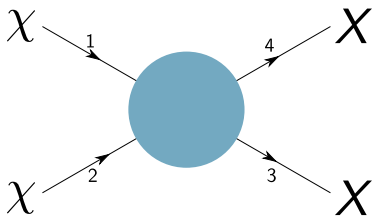

Figure 4 – Annihilation of a DM self-annihilating species χ into a pair of SM particles X. The teal solid circle (●) denotes some unknown interaction. Source: By the author.

It can be shown from the formalism of the collision integrals in the Boltzmann equation (12) that the annihilation rate of DM particles is:

$$\Gamma = n_\chi \langle \sigma v_{\text{Møl}} \rangle \tag{8}$$

where n_χ is the number density of DM particles, $\langle \sigma v_{\text{Møl}} \rangle$ is the thermally averaged cross-section and $v_{\text{Møl}}$ is the Møller velocity. By definition:

$$\langle \sigma v_{\text{Møl}} \rangle = \frac{\int \sigma v_{\text{Møl}} dn_1^{\text{eq}} dn_2^{\text{eq}}}{\int dn_1^{\text{eq}} dn_2^{\text{eq}}}. \tag{9}$$

which can be intuitively interpreted as accounting for the spread of accessible energies of the DM particles when they interact with SM particles, that are considered in thermal equilibrium with photons.

In this context of thermal dark matter, DM decoupled from the SM particles bath early in the Universe's history, so that they are effectively free-streaming towards us since then and exists today as a *thermal relic* of the primordial universe. The *thermal relic* cross-section for DM interactions (12) annihilating into SM states that can account for the cosmological DM abundance mentioned in Section 1 is $\langle \sigma v_{\text{Møl}} \rangle = 3 \times 10^{-26}\,\text{cm}^3\,\text{s}^{-1}$. [3] This value set an important target cross-section for our modelling process in Section 6.

Now, let's assume that DM annihilates uniquely into a known SM state ($b\bar{b}, \tau^+\tau^-, \gamma\gamma, \dots$) with a thermally averaged cross-section $\langle \sigma v \rangle_i$. Then, by eq. (8), the annihilation rate per particle is:

$$\Gamma = \frac{\rho[r(s,\theta)]}{m_\chi} \langle \sigma v \rangle_i \tag{10}$$

where m_χ is the DM particle mass and $\rho[r(s,\theta)]$ is the density of DM particles at a distance r from the galactic center (GC), parameterized in terms of the distance s between the Sun and the DM particles and the angle θ between GC and the DM particles as seen from the Sun. These coordinates are depicted in Figure 2. If we confine our attention to a volume dV, the total annihilation rate in this volume is obtained through multiplication of equation (10) with the total number of particles in dV:

$$\Gamma_{\text{tot}} = \left(\frac{\rho[r(\ell,b)]}{m_\chi} \langle \sigma v \rangle_i \right) \times \left(\frac{\rho[r(\ell,b)]}{2m_\chi} dV \right) \tag{11}$$

where the factor 2 accounts for the need of two particles in the annihilation process. Let us consider the total annihilation rate expected to be observed on our line of sight (los) if we

[3] For notation brevity, we will denote $\langle \sigma v_{\text{Møl}} \rangle$ simply as $\langle \sigma v \rangle$.

assume that the byproducts are emitted isotropically:

$$\begin{aligned}\Gamma_{\rm los} &= \int_0^\infty ds \frac{1}{4\pi s^2}\left(\frac{\rho[r(s,\theta)]^2}{2m_\chi^2}\langle\sigma v\rangle_i\right) s^2 d\Omega \\ &= \frac{1}{4\pi}\int_0^\infty ds\left(\frac{\rho[r(s,\theta)]^2}{2m_\chi^2}\langle\sigma v\rangle_i\right) d\Omega\end{aligned} \tag{12}$$

Now, to get the total photon flux we must contemplate the photon multiplicity dN/dE_γ of each annihilation at a given photon energy E_γ – including secondary photons produced in cascade. Thereby, the differential photon flux $d\Phi/dE_\gamma$ expected in the line of sight, at an angle θ from the GC, of the observer is:

$$\frac{d\Phi}{dE_\gamma} = \frac{1}{4\pi}\frac{\langle\sigma v\rangle_i}{2m_\chi^2}\frac{dN}{dE_\gamma}\int_{\Delta\Omega} d\Omega \int_0^\infty ds\rho[r(s,\theta)]^2 \tag{13}$$

where $\Delta\Omega$ is the solid-angle aperture of the region being observed.

Importantly, all the astrophysical or *spatial* uncertainties are absorbed by the J-factor:

$$J = \frac{1}{\Delta\Omega}\int_{\Delta\Omega} d\Omega \int_0^\infty ds\rho[r(s,\theta)]^2 \tag{14}$$

The larger the J-factor, the more we expect the occurrence of annihilation events from DM particles. For instance, the J-factors (2) for dwarf galaxies are roughly $J \sim 10^{19-20}\,\mathrm{GeV}^2/\mathrm{cm}^5$ and for the Andromeda Galaxy, $J \sim 10^{20}\,\mathrm{GeV}^2/\mathrm{cm}^5$. For a circular region of 1° centered on our own Galactic Center (GC), $J \sim 10^{22-24}\,\mathrm{GeV}^2/\mathrm{cm}^5$. The high J-factor associated with the GC, along with precise models of the astrophysical background emission of photons, is one of the main reasons we focus our analysis in the Galactic Center. The astrophysical environment of the GC will be discussed in Section 3.

In a similar way, we can think of the term:

$$\frac{\langle\sigma v\rangle_i}{2m_\chi^2}\frac{dN}{dE_\gamma}$$

as defining the *spectral* properties of the signal. In our case, we will consider $\langle\sigma v\rangle_i$ and m_χ^2 as free parameters of our model and use the multiplicities of photons, primary and secondary, as calculated in (13).

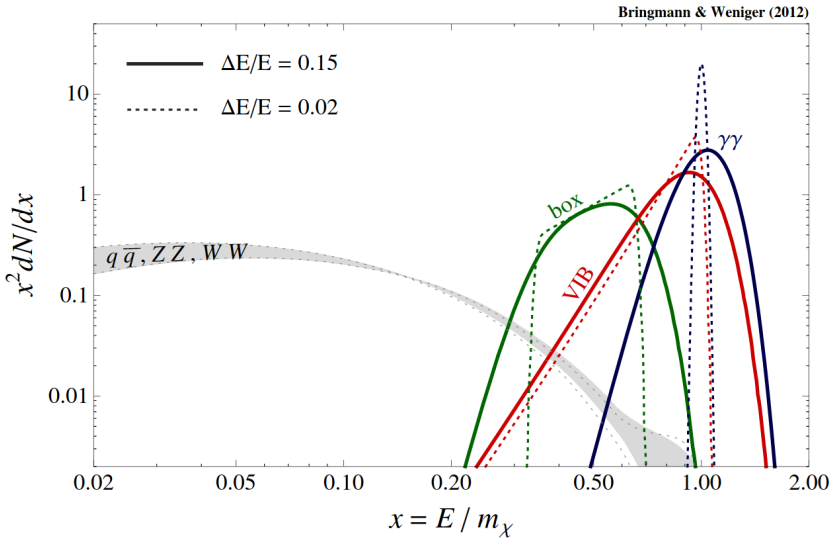

Figure 5 – Multiplicites of final state for annihilations into quarks, gauge bosons and photons. The multiplicities where multiplied by x^2 to enhance spectral features. Source: BRINGMANN, T.; WENIGER, C. (14)

To further understand this spectral component, we show, in Figure 5, the expected flux for different annihilation channels. Observe that, instead of plotting the pure energy dependency of the flux, it is convenient to restrict our attention to the dependency on a more suitable coordinate $x := E_\gamma/m_\chi$, that factors out the DM mass effect on the produced photon energies. Additionally, the flux is multiplied by x^2 to enhance spectral features.

In interpreting Figure 5, we first focus in the case where DM annihilates directly into one or two photons: $\chi + \chi \to \gamma + X$, where $X = \gamma, Z, H$ or some other neutral particle. In this case, by four-momentum conservation:

$$p_{\chi,1} + p_{\chi,2} = p_\gamma + p_X \iff 2\sqrt{m_\chi^2 c^4 + \mathbf{p}_\chi^2 c^2} = E_\gamma + \sqrt{E_\gamma^2 + m_X^2 c^4} \tag{15}$$

In the non-relativistic limit for the DM species $|\mathbf{p}_\chi| \ll m_x c$, we have:

$$E_\gamma = m_\chi c^2 \left(1 - \frac{m_X^2}{4m_\chi^2}\right) \overset{c=1}{\iff} x = \left(1 - \frac{m_X^2}{4m_\chi^2}\right) \tag{16}$$

This kind of annihilation corresponds, in the energy spectrum, to a narrow line at $m_\chi x$, where x was defined at eq. (16). In Figure 5, it is shown for the case of a photon ($m_X = 0, x = 1$), although the authors include an energy dispersion to check the possibility of detection.

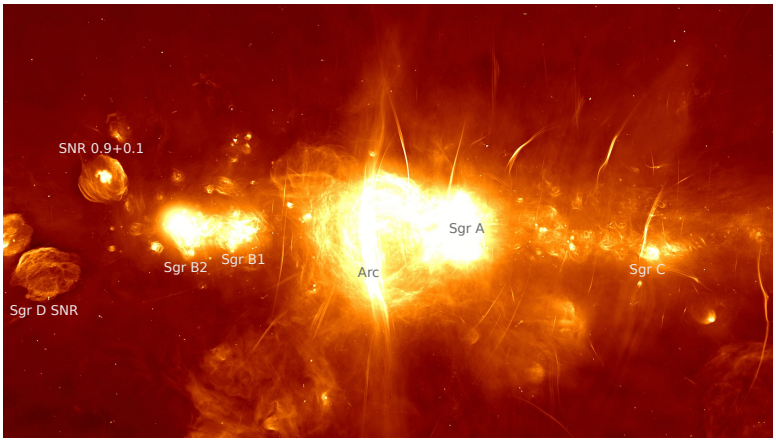

Figure 6 – The galactic center as imaged by the MeerKAT Collaboration. Source: By the author.

Now, the box shaped feature in Figure 5 is a signature of cascade decays of DM particles annihilating to neutral intermediate states $\chi + \chi \to \phi + \phi$ which subsequently decay directly into photons $\phi \to \gamma + \gamma$ or via final state radiation into photons (*e.g.* $\phi \to l^+ + l^- + \gamma$, for some lepton l) (14).

Finally, the gray band in Figure 5, is the expected flux if DM annihilates to quarks, leptons, Higgs and weak gauge bosons, that produce secondary photons after hadronization and subsequent decay. Compared with the the line and box shaped spectral features, this is the most featureless one. However, because lines and cascade decays are strongly suppressed (they normally involve high order processes in theories), we will focus on DM decaying to quarks, particularly the *bottom* ($b\bar{b}$) quarks.

3 The Galactic Center (GC) region

The Galactic Center (GC) is the rotational center of our Galaxy, the Milky Way, and is located, according to stellar kinematics observations, at a distance $R_\odot \approx 8.3\,\mathrm{kpc}$. Our interest, however, is the myriad of objects that populate the inner $\approx 5^\circ$ around the GC. For instance, the GC is spatially coincident with a strong radio source, Sgr A*, that is though to be a black hole with mass $4.4 \times 10^6\,\mathrm{M}_\odot$ (15). Besides that, the inner GC region contains unexplained populations of young early-type stars and many supernova remnants (SNRs), as shown in Figure 6. Additionally, it may also encompass residues of the Fermi Bubbles (16), two large cocoons emanating from the GC, whose existence is attributed to past activity of the central black hole.

Briefly, two aspects of the GC are of utter importance to us. First, the fact that it

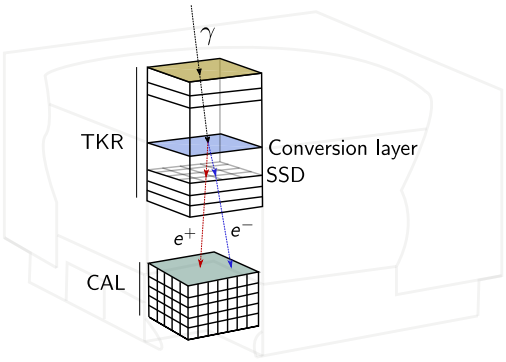

Figure 7 – The LAT Instrument. Source: By the author.

may densely concentrate dark matter particles whose annihilation can be detected on Earth as gamma rays. Second, because the GC environment harbors many objects that are point-like or diffuse sources of gamma rays that can be confused with DM annihilation byproducts. Therefore, the emission of these objects needs to be properly subtracted from the entirety of gamma rays detected. We will discuss this subtraction on Section 6.

4 The LAT instrument aboard Fermi Gamma-ray Space Telescope

4.1 Properties and detection methodology

The LAT (Large Area Telescope) instrument is a pair conversion detector on board of the Fermi Gamma-ray Space Telescope. Covering the energy range from 20 MeV to $\gtrsim 300$ GeV, LAT has a large collecting area ($\approx 0.8\,\mathrm{m}^2$ on axis), imaging capabilities over a large FOV (2.4 sr) and a flexible and well documented event reconstruction procedure. Additionally, many data analysis environments have emerged since the mission onset, including the `fermipy` library that we extensively used during this work.

Concisely, following the depiction in Figure 7, the detection proceeds as follows: gamma rays penetrate into the detector and interact with a tungsten conversion layer to produce an electron-positron pair; the pair is tracked along its way to the bottom of the tracker (TKR) by charge-sensitive elements (SSDs). When the pair hits the bottom section of the instrument, it deposits the entirety of its energy on a CsI calorimeter (CAL). Besides measuring the energy, the calorimeter does also track the pair.

4.2 Instrument Response Functions (IRFs) and event reconstruction

The direction of incidence and energy of the incoming gamma ray needs to be recovered from the imprint left by the electron-positron pair on the tracker and the calorimeter. The translation between hits in the various part of the LAT and the identification of the event type (*e.g*, astrophysical photon or noise) along with its characterization is called event reconstruction.

As part of the event reconstruction process, the LAT instrument team discriminate subsets of events based on the probability that the events were generated by a photon (*photon probability*) and the quality of their reconstruction. These selections are used to separate events into *event classes*, with each class characterized by its own set of Instrument Response Functions (IRFs).

An Instrument Response Function (IRF) is the mapping between the incoming photon flux and the detected events parameters, as diagrammatically shown in Figure 8. To evaluate the IRFs, a dedicated Monte Carlo simulation covering all possible photon inclination angles and energies is performed. The LAT IRFs are modelled by splitting the response in three contributions: the effective area, the point spread function and the energy dispersion. The parameters describing each part of the IRFs are fixed by the LAT team.

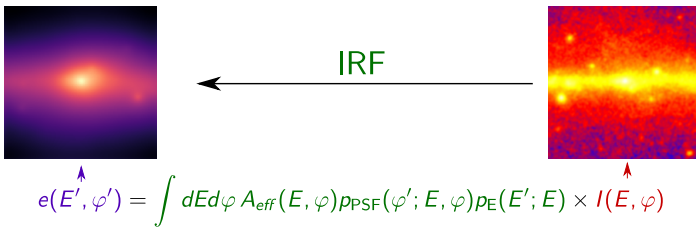

Figure 8 – A diagrammatic depiction of LAT IRFs. Source: By the author.

As we mentioned, events are separated into event classes, with each class possessing its own set of IRFs. Furthermore, within each event class, events are subdivided into event types that are based on individual event topologies. For instance, if the photon converted in the first 12 thin conversion layers or in the 4 last thick layers, the events are classified as `FRONT` or `BACK`, respectively.

The nested hierarchy of event classes and types allows the data analyst to select events with the most suited balance between instrument response and photon counts. For example, by choosing event types with narrow PSF and low background contamination, we may constrain

too much the available list of photons. By the other hand, if selection criteria are too loose, data may be highly contaminated by events not associated with astrophysical gamma rays.

5 Statistical framework

The main LAT data product is a list of events with reconstructed physical parameters, photon probabilities and the quality of the reconstruction. Since we employ a large dataset, with an unmanageable amount of distinct energies and spatial coordinates of gamma rays sources, binning the data in spatial and energy categories is mandatory.

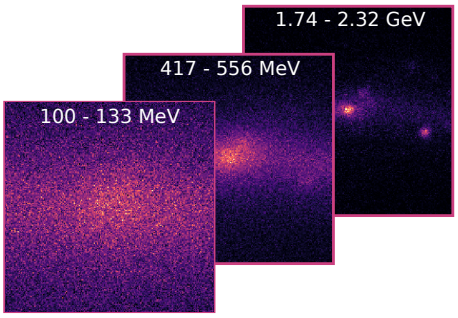

Figure 9 – Spatial and energy binning representation for 3 energy bins. Source: By the author.

After that, we assume that the photon counts in each spatial-energy bin is independent. Further, we suppose that the counts in each bin, henceforth spatially indexed by $i = 1, \ldots, n$ and energetically by $j = 1, \ldots, m$, to be $D_{ij} \sim \text{Poisson}(\mu_{ij})$, where μ_{ij} is the expected number of counts in the (i, j)-th bin during the observation period. Therefore, with these assumptions, the log-likelihood of the model given the observed $d_{11}, \ldots, d_{nm}$ counts is:

$$\log \mathcal{L}(\mu_{11}, \ldots, \mu_{nm}) = \sum_{i,j} \{d_{ij} \log \mu_{ij} - \log d_{ij}! - \mu_{ij}\} \tag{17}$$

Now, we further split the Poisson rates μ_{ij} in so-called *templates* P_{ij}^m, each one accounting for a fraction of the detected gamma rays. More specifically, templates are fitting components consisting of a spectral part, that models how the number of counts associated with it depends on energy, and a spatial part, that models whether the gamma ray source is point-like, extended or diffuse. Accordingly, we write:

$$\mu_{ij} = \sum_m f_m P_{ij}^m \tag{18}$$

where m indexes the adopted templates and f_m are normalization constants fixed during fitting. We describe the adopted templates in Section 6.

The templates' parameters, including, for instance, spectral indexes of sources with power law spectral energy distribution or coordinates of point sources, are estimated by the maximum-likelihood method. The maximization is performed in two iterative steps:

1. Optimization: we fix a fraction $N_{\rm pred}/N_{\rm total}$ of the total detected counts. Then, we free the normalization of the brightest sources whose sum of fractional counts relative to the total is approximately equal to $N_{\rm pred}/N_{\rm total}$. After that, the normalization parameters of these sources are simultaneously fit. The remaining sources parameters are kept fixed. Subsequently, each source that was skipped in the last step has its normalization parameter fit individually. In the last step, all sources with TS > 25[4] have their normalization and shape parameters fit individually. This whole step is performed for $N_{\rm pred}/N_{\rm total} = (0.5, 0.9, 0.99)$.

2. Fit: we fit all sources parameters in intervals of significance, as determined from the TS. That is, we fix an interval $\mathcal{I}$ of TS, free all the parameters of every source with TS $\in \mathcal{I}$ and fix the parameters of all remaining sources. Then, we fit the parameters of sources with TS in $\mathcal{I}$. We proceed in this manner for the following intervals: $[300, +\infty)$, $[200, 300]$, $[100, 200]$, $[64, 100]$, $[49, 64]$ and $[25, 49]$.

6 Modelling

For our analysis of the existence and interpretation of the GeV Excess, we employed the same data interval as used in the LAT Collaboration article on the subject (16). The study is based on 6.5 years of LAT data recorded between 2008 August 4 and 2015 January 31 (Fermi Mission Elapsed Time 239557418 s - 444441067 s).

Additionally, following the guidelines of the LAT instrument team, we employed LAT P8R3 IRFs with event class `SOURCE` and event types both `FRONT` and `BACK`.

[4] TS is an acronym for *test statistic*. It is related to the likelihood ratio test (the most powerful test for comparing simple hypothesis) and, more generally, to the Wilks' theorem (17).

We use a square spatial binning scheme with bin size of $\delta = 0.05\,^\circ$. The analyzed region of interest (ROI) covers the galactic longitudes from $\ell = -5\,^\circ$ to $\ell = 5\,^\circ$ and galactic latitudes from $b = -5\,^\circ$ and $b = 5\,^\circ$.

To model point and extended sources in the ROI we use the catalog `4FGL-DR2` provided by the Fermi Collaboration as part of the 10 year data release. Despite using the initial values defined in the catalog files, we allow normalization and shape parameters of sources to vary. Spatial parameters of the 30 brightest sources were also adjusted in a relocalization step adopted in the full fitting procedure, depicted schematically in Figure 10.

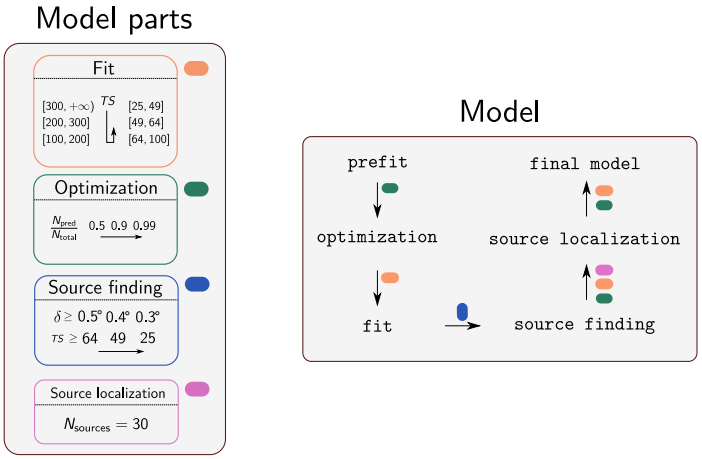

Figure 10 – Model parts and model construction description. Text in typewriter typeface (*e.g.* `prefit`) are checkpoints. Arrows indicate a modelling step where each model part, as depicted with a colored rectangle with rounded corners, was used. The order of use of each model part follows the direction of the arrow. Source: By the author.

We also employed a source finding step to find statistically significant new point sources. Only sources with a minimum TS of 25 and at angular distances (δ) from previous sources greater than certain thresholds (see Figure 10) were selected to avoid source confusion and model overfitting. This step is inspired by the procedure adopted in (16).

Spatially, we modelled the Fermi Bubbles with a non-flat template, shown in Figure 11b, extracted from the Fermi Collaboration analysis of the GeV Excess. There is, however, evidences that the Fermi Bubbles emission is spatially flat (6). For the spectral part, we used a log-parabola model with parameters fixed at the values defined in (18).

Now, for the DM annihilation modelling, we adopted a standard NFW profile for the spatial part, shown in Figure 11a. For the spectral part, we set the annihilation channel as $b\bar{b}$

with branching ratio $\mathsf{BR} = 1$ and used the photon multiplicities calculated in (13).

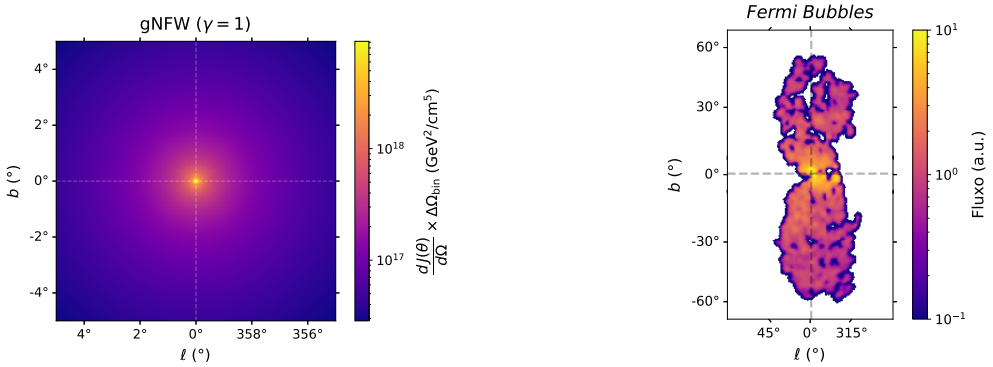

(a) DM Template. Source: By the author.

(b) Fermi Bubbles template. Source: ACKERMANN, M. *et al.*(16)

Figure 11 – Adopted templates for DM annihilation and the Fermi Bubbles.

An important part of the model is the diffuse emission template. Diffuse emission is mainly related to the production of gamma rays from the decay of neutral pions (π^0), the Inverse Compton Scattering (ICS) of photons in the interstellar radiation field (ISRF) and the *bremsstrahlung* of electrons in the interstellar medium (ISM). However, the most recent templates of diffuse emission can contain parts of the emission attributed to the Fermi Bubbles or the annihilation of DM and, therefore, can cause over-subtraction of the DM signal. For this reason, we employed the diffuse emission model from Fermi Pass 6 referred as `p6v11`, the last model released by the Fermi Collaboration that does not include the Fermi Bubbles or, possibly, DM associated gamma ray emission.

7 Results and discussion

We show in Figure 12 the fractional residuals before (12a) and after (12b) the addition of the DM annihilation template. Observe that, before the DM template addition, there is a pronounced and unmodelled positive residual around 10 GeV, consistent with the energy scale of the GeV Excess (16). The excess almost completely disappears after the addition of the DM template. However, there emerges a new residual in energies greater than ≈ 40 GeV that is probably associated with the shift of the Fermi Bubbles template to low energies after the addition of DM template.

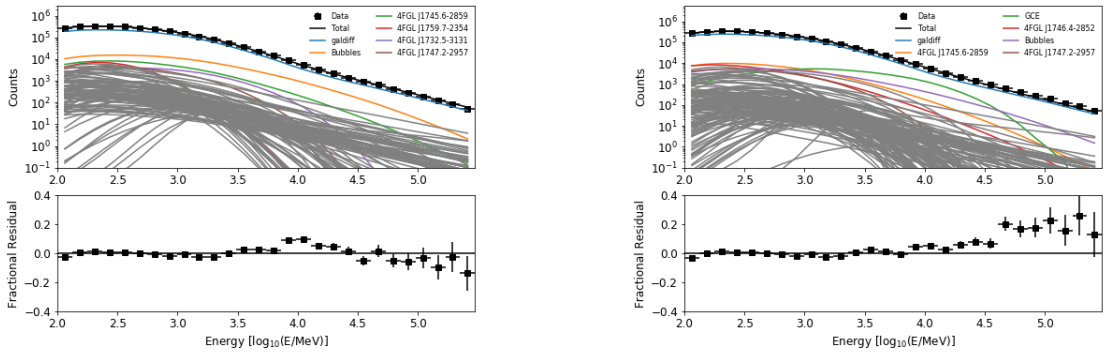

(a) Before addition of DM template.

(b) After addition of DM template.

Figure 12 – Fractional residual before (a) and after (b) the addition of the DM template. Source: By the author.

In addition, we also characterized the spatial morphology of the residual, as shown in Figure 13. Notice how, between 2.51 GeV and 5.01 GeV, the same energy scale of the positive residual in Figure 12a, the photon excess distributes with approximate radial symmetry around the GC. This distribution seems consistent with our description of DM halos as been spherically symmetric.

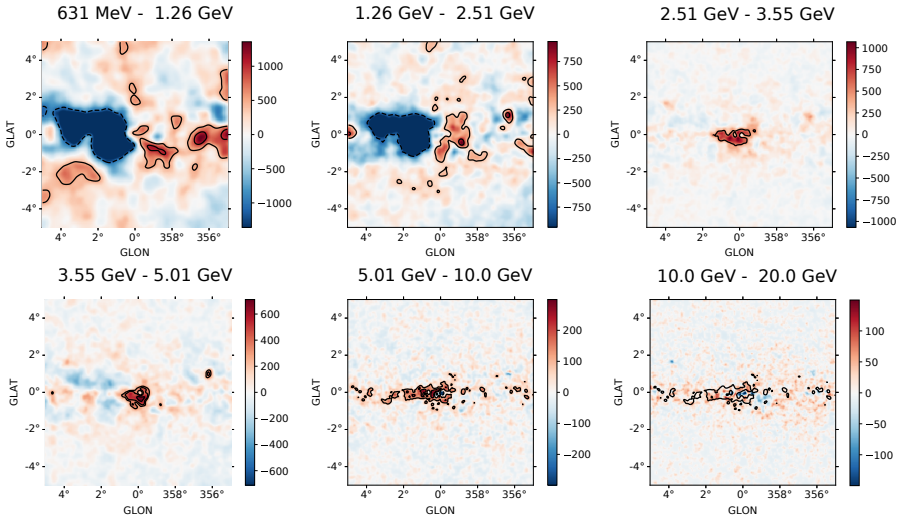

Figure 13 – The morphology of the residual before addition of the DM template in energy bins between 631 MeV and 20.0 GeV. Source: By the author.

To conclude, we show in Table 1 the results of the fit after the addition of the DM template. Although the mass scale is compatible with some reported upper limit results (16), errors could not be estimated because of convergence issues in the likelihood maximization – probably related to poor model constraining.

Table 1 – Fit results after the addition of the DM template.

m_χ	$194 \pm \texttt{nan}$ GeV
$\langle \sigma v \rangle$	$2.576 \times 10^{-26} \pm \texttt{nan}$ cm^3 s^{-1}

Source: By the author.

8 Conclusions

In this work, we studied the dark matter paradigm and aspects of DM indirect detection to substantiate an analysis of the GeV Excess in terms of self-annihilating dark matter. The DM paradigm initially emerged to explain dynamical observations but was soon realized as been closely related to cosmology and particle physics. Despite evidences of its existence, no claim of DM detection has been definitively accepted by the scientific community. We focused on characterization of radiation as a byproduct of DM annihilation and how it could be detected using the Fermi Gamma-ray Space Telescope, of whom we minutely described the principles of working. As a result of our analysis, we recovered the expected GeV excess at ~ 5 GeV and characterized it spatially, showing its morphology is consistent with a spherically symmetric DM halo. Because of poor model constraining that probably generated many degenerescences in the likelihood optimization procedure, our fit results could only estimate the free parameters – m_χ and $\langle \sigma v \rangle$ – values, but not its errors. Despite of this problem, that we firmly believe can be solved with a new approach to the fit (employing more rigidly the cataloged parameters values and avoiding simultaneous fit of spectrally similar sources), the mass and cross-section estimates are consistent with upper limit results reported in the literature.

References

1 ZWICKY, F. Die Rotverschiebung von extragalaktischen Nebeln. *Helvetica Physica Acta*, v. 6, p. 110–127, 1933.

2 LISANTI, M. Lectures on dark matter physics. *In: TASI 2015. New frontiers in fields and strings*, Singapore: World Scientific, 2016.

3 BOVY, J. *Dynamics and Astrophysics of Galaxies*. 2020. Available on: ⟨http://astro.utoronto.ca/~bovy/AST1420/notes-2019/index.html⟩. Accessed on: Mar. 2021.

4 RUBIN, V. C.; FORD W. K., J.; THONNARD, N. Rotational properties of 21 SC galaxies with a large range of luminosities and radii, from NGC 4605 (R=4kpc) to UGC 2885 (R=122kpc). *Astrophysical Journal*, v. 238, p. 471–487, June 1980.

5 AGHANIM, N. *et al.* Planck 2018 results. *Astronomy Astrophysics*, EDP Sciences, v. 641, p. A6, Sept. 2020.

6 CALORE, F.; CHOLIS, I.; WENIGER, C. Background model systematics for the Fermi GeV excess. *Journal of Cosmology and Astroparticle Physics*, IOP Publishing, v. 2015, n. 03, p. 038–038, Mar. 2015.

7 HOOPER, D.; GOODENOUGH, L. Dark matter annihilation in the Galactic Center as seen by the Fermi Gamma Ray Space Telescope. *Physics Letters B*, Elsevier BV, v. 697, n. 5, p. 412–428, Mar. 2011.

8 BATTAGLIA, G. *et al.* The radial velocity dispersion profile of the Galactic halo: constraining the density profile of the dark halo of the Milky Way. *Monthly Notices of the Royal Astronomical Society*, Oxford University Press (OUP), v. 364, n. 2, p. 433–442, Dec. 2005.

9 SPRINGEL, V. *et al.* The Aquarius Project: the subhaloes of galactic haloes. *Monthly Notices of the Royal Astronomical Society*, Oxford University Press (OUP), v. 391, n. 4, p. 1685–1711, Dec. 2008.

10 NAVARRO, J. F.; FRENK, C. S.; WHITE, S. D. M. The structure of cold dark matter halos. *The Astrophysical Journal*, American Astronomical Society, v. 462, p. 563, May 1996.

11 BUSCHMANN, M. *et al.* Foreground mismodeling and the point source explanation of the Fermi Galactic Center excess. *Physical Review D*, American Physical Society (APS), v. 102, n. 2, July 2020.

12 KOLB, E.; TURNER, M. *The Early Universe*. [S.l.]: Avalon Publishing, 1994. (Frontiers in physics).

13 JELTEMA, T. E.; PROFUMO, S. Fitting the gamma-ray spectrum from dark matter with DMFit: GLAST and the Galactic Center Region. *Journal of Cosmology and Astroparticle Physics*, IOP Publishing, v. 2008, n. 11, p. 003, Nov. 2008.

14 BRINGMANN, T.; WENIGER, C. Gamma ray signals from dark matter: Concepts, status and prospects. *Physics of the Dark Universe*, Elsevier BV, v. 1, n. 1-2, p. 194–217, Nov. 2012.

15 GENZEL, R.; EISENHAUER, F.; GILLESSEN, S. The Galactic Center massive black hole and nuclear star cluster. *Reviews of Modern Physics*, American Physical Society (APS), v. 82, n. 4, p. 3121–3195, Dec. 2010.

16 ACKERMANN, M. *et al.* The Fermi Galactic Center GeV Excess and Implications for Dark Matter. *The Astrophysical Journal*, American Astronomical Society, v. 840, n. 1, p. 43, May 2017.

17 BOLFARINE, H.; SANDOVAL, M. *Introdução à inferência estatística*. [S.l.]: SBM, 2001. (Coleção Matematica Aplicada).

18 ACKERMANN, M. *et al.* The spectrum and morphology of the Fermi Bubbles. *The Astrophysical Journal*, American Astronomical Society, v. 793, n. 1, p. 64, Sept. 2014.